

THERMO FLUID DYNAMICS AND CHAMBER AEROSOL BEHAVIOR FOR THIN LIQUID WALL UNDER IFE CYCLIC OPERATION

A. R. RAFFRAY,*† S. I. ABDEL-KHALIK,‡ D. HAYNES,§ F. NAJMABADI,|| P. SHARPE,#
M. YODA,‡ M. ZAGHLOUL,|| and ARIES-IFE TEAM

† *University of California, San Diego, Mechanical and Aerospace Engineering Department and Center for Energy Research, EBU-II, Room 460, La Jolla, California 92093-0417*

‡ *Georgia Institute of Technology, School of Mechanical Engineering, Atlanta, Georgia 30332-0405*

§ *University of Wisconsin, Fusion Technology Institute, 1500 Engineering Drive, Madison, Wisconsin 53706-1687*

|| *University of California, San Diego, Center for Energy Research, EBU-II, Room 460, La Jolla, California 92093-0417*

Idaho National Engineering and Environmental Laboratory, Fusion Safety Program, EROB E-3 MS 3815, Idaho Falls, Idaho 83415-3815

Received June 23, 2003

Accepted for Publication April 29, 2004

A thin-liquid-wall configuration combines the attractive features of a solid wall with the advantages of a renewable armor to accommodate the threat spectra produced by inertial fusion energy targets. Key design issues for successful implementation of the thin-liquid-film wall protection schemes are the reestablishment of the thin liquid armor and the state of the chamber environment prior to each shot relative to the requirements imposed by the driver and target thermal and injection control. Experimental and numerical studies have been conducted to examine the fluid dynamic aspects of thin-liquid-

film protection systems with either radial injection through a porous first wall or forced flow of a thin liquid film tangential to a solid first wall. Analyses were also conducted to help assess and understand key processes influencing the chamber environment, including ablation mechanisms that could lead to aerosol formation and the behavior of such aerosol in the chamber. Results from these studies are described in this paper.

KEYWORDS: *inertial fusion energy, wetted wall, ablation mechanisms*

I. INTRODUCTION

A thin liquid wall (or wetted wall) combines the attractive features of a solid wall (such as robust mechanical design and efficient energy recovery) with the advantages of a renewable armor to accommodate the X-ray and ion threat produced by inertial fusion energy (IFE) target explosions. In this configuration, part of the thin-liquid-film armor evaporates under the incident X-ray and ion energy deposition fluxes. Such a configuration has been considered previously, for example, in the PulseStar reactor study¹ and, more recently, in the PROMETHEUS reactor study.² Key design issues for successful implementation of such concepts are the reestablishment of the thin liquid armor and the state of the

chamber environment prior to each shot relative to the requirements imposed by the driver beam propagation and focusing requirements, as well as the target thermal integrity and injection control. In determining the conditions of the chamber gas and/or vapor prior to each shot, it is important to consider the possible presence of aerosol. The major processes involved in chamber clearing are those providing the source terms for aerosol formation (both from the high power deposition at the wall and from subsequent in-flight recondensation), the aerosol behavior between shots, and condensation to the wall.

These issues were analyzed in detail as part of the ARIES-IFE study³ for different driver and target combinations; this paper summarizes the key results from the study. First, the example target threat spectra are described. Next, an assessment of film reestablishment and coverage is presented for both the wetted-wall concept

*E-mail: raffray@fusion.ucsd.edu

with normal injection through a porous wetted wall and the forced-film-flow concept with tangential injection of the liquid along the wall surface. Film detachment and droplet formation are discussed. A scoping analysis of condensation under IFE conditions is then presented. Finally, an analysis of aerosol formation and behavior is summarized including characterization of source terms and an initial estimate of size and density of aerosol remnants prior to each shot. The chamber conditions at that time must be compatible with driver firing and target injection requirements. These are discussed in more detail in Ref. 3.

Lead and flibe (LiF/BeF_2) have been considered in recent IFE concepts, such as the PROMETHEUS wetted-wall concept² and the HYLIFE thick-liquid-wall concept,⁴ and are considered as example liquids in the analysis presented here.

II. TARGET THREAT SPECTRA

The ARIES-IFE study considered two different types of target:

1. a direct-drive target, whereby the driver energy is deposited directly on the target
2. an indirect-drive target utilizing a radiation hohlraum enclosure. The X rays resulting from the driver beam interaction with the hohlraum material are deposited on the deuterium-tritium (D-T) target pellet inside the hohlraum, which leads to its implosion and ignition.

The direct-drive cryogenic target is much more sensitive to chamber conditions than the indirect-drive target, which is thermally protected by its massive hohlraum.³ For a wetted-wall configuration, significant evaporation and ablation of the wall are expected from the photon and ion energy deposition, which makes the reestablishment of the chamber environment prior to each shot to a state compatible with direct-drive target requirements extremely challenging. For this reason, the focus of the work presented here is on the more robust indirect-drive target, which is usually coupled with a heavy-ion driver.

For comparison, the energy partitioning for two example targets considered in the ARIES-IFE study [a 154-MJ Naval Research Laboratory (NRL) laser direct-drive target^{5,6} and a 458-MJ heavy-ion indirect-drive target^{7,8}] are shown in Table I; these are based on LASNEX calculations.⁸ The photons and ions are the major threats to the chamber wall. Neutrons penetrate much more deeply into the structure and blanket and, as such, are much less of a threat to the chamber wall. The corresponding photon spectra for both targets are shown in Fig. 1. A major difference between the direct-drive and indirect-drive threat spectra is the large energy fraction carried by photons in the indirect-drive case (25%) as opposed to the

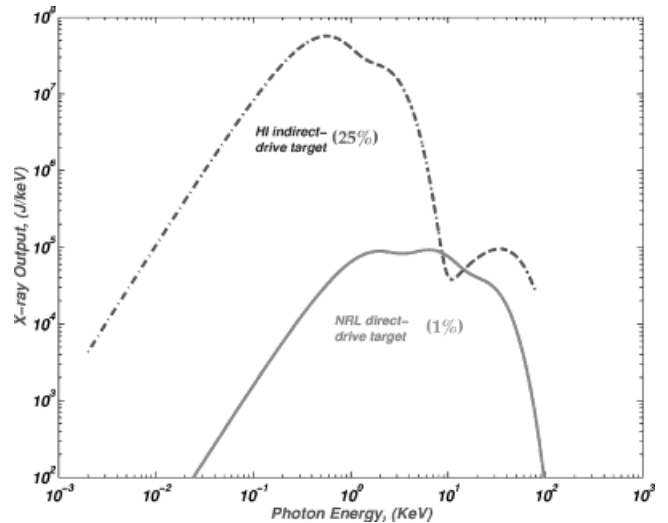


Fig. 1. Photon spectra from NRL 154-MJ direct-drive target and Lawrence Livermore National Laboratory 458-MJ heavy-ion-beam indirect-drive target.⁷

direct-drive case (1%). Further, the X-ray spectrum of the indirect-drive target is dominated by soft (<1 -keV), shallowly penetrating photons, which makes the deliberate evaporation required in wetted-wall protection schemes even more attractive. The photon energy deposition time is very small (typically subnanoseconds), which results in extremely large heat fluxes on the wall, thereby causing substantial wall ablation and evaporation. Detailed information on the corresponding ion spectra for both targets can be found in Ref. 7. Here, the ion spectra for the burn products (fast ions) and the debris ions for the indirect-drive target (assumed in this analysis) are shown in Figs. 2 and 3, respectively.

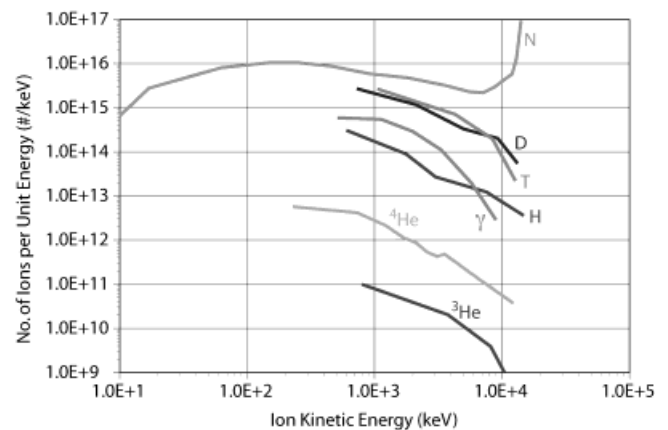


Fig. 2. Fast ion spectra from Lawrence Livermore National Laboratory 458-MJ indirect-drive target.⁷

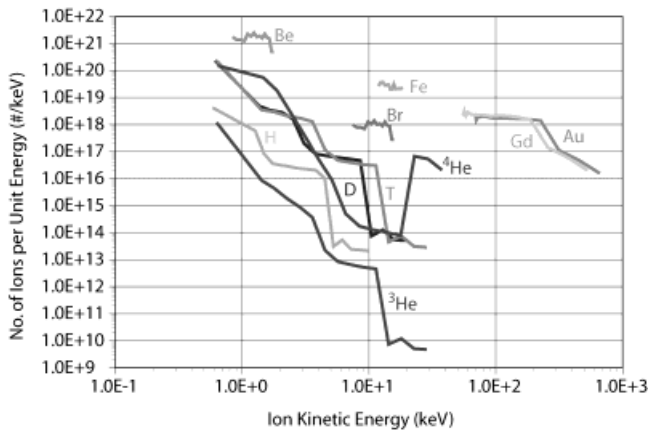


Fig. 3. Debris ion spectra from Lawrence Livermore National Laboratory 458-MJ indirect-drive target.⁷

III. FILM DYNAMICS

Experimental and numerical studies have been conducted to examine the fluid dynamic aspects of thin-liquid-film protection systems with either radial injection through a porous first wall (hereafter referred to as the “wetted-wall” design) or forced flow of a thin liquid-film tangential to a solid first wall (hereafter referred to as the “forced-film” design). Previous work on liquid film flow on vertical and upward-facing surfaces has shown that for all IFE coolants of interest with surface contact angles ranging from 0 to 90 deg, dry patch formation can be prevented by maintaining the film thickness and flow velocity above ~1 mm and 1 m/s, respectively.^{9,10} Hence, for both the wetted-wall and forced-film designs, our efforts have been focused on examining the behavior of the liquid film on the downward-facing surfaces (upper section) of the reactor cavity, where virtually no work has heretofore been done.

Among the critical questions needed to establish the viability of the wetted-wall concept are the following:

1. Can a stable liquid film be maintained on the upper section of the chamber?
2. Can the film be reestablished over the entire cavity surface prior to the next target explosion?
3. Can a minimum film thickness be maintained to prevent dry patch formation and provide adequate protection during the next target explosion?

To this end, a level contour reconstruction method has been used to track the three-dimensional evolution of the liquid-film surface on porous downward-facing walls with different initial film thickness, liquid injection velocity through the porous wall, surface disturbance amplitude, configuration and mode number, surface inclination angle, liquid properties, and mass exchange rate between the liquid and chamber “gas” due to evaporation and/or condensation. Calculations have been performed to examine the effect of these variables on the transient three-dimensional topology of the film free surface, the frequency of liquid drop formation and detachment, the size of the detached droplets, and the minimum film thickness prior to droplet detachment. Detailed descriptions of the numerical model and level contour reconstruction method can be found in a companion paper.¹¹ The results of the calculations have been used to develop nondimensional “generalized charts,” which make it possible for system designers to establish “design windows” for successful implementation of the wetted-wall concept. A preliminary experimental investigation aimed at validating the model has also been performed.

Typical results showing the evolution of the free surface for a liquid lead film on a horizontal downward-facing surface are shown in Fig. 4. The film is assumed to be 700 K with an initial thickness of 1.0 mm and an injection velocity of 1.0 mm/s. A random initial

TABLE I
Energy Partitioning for 154-MJ NRL Direct-Drive Target and 458-MJ Heavy-Ion Indirect-Drive Target*

	NRL Direct-Drive Target (MJ)	Heavy-Ion Indirect-Drive Target (MJ)
X rays	2.10 (1.4%)	115 (25%)
Neutrons	109 (71%)	316 (69%)
Gammas	0.0089 (0.006%)	0.36 (0.1%)
Burn product fast ions	19.5 (13%)	8.43 (2%)
Debris ions kinetic energy	22.1 (14%)	18.1 (4%)
Residual energy	1.29	0.57
Total	154	458

*From Ref. 7.

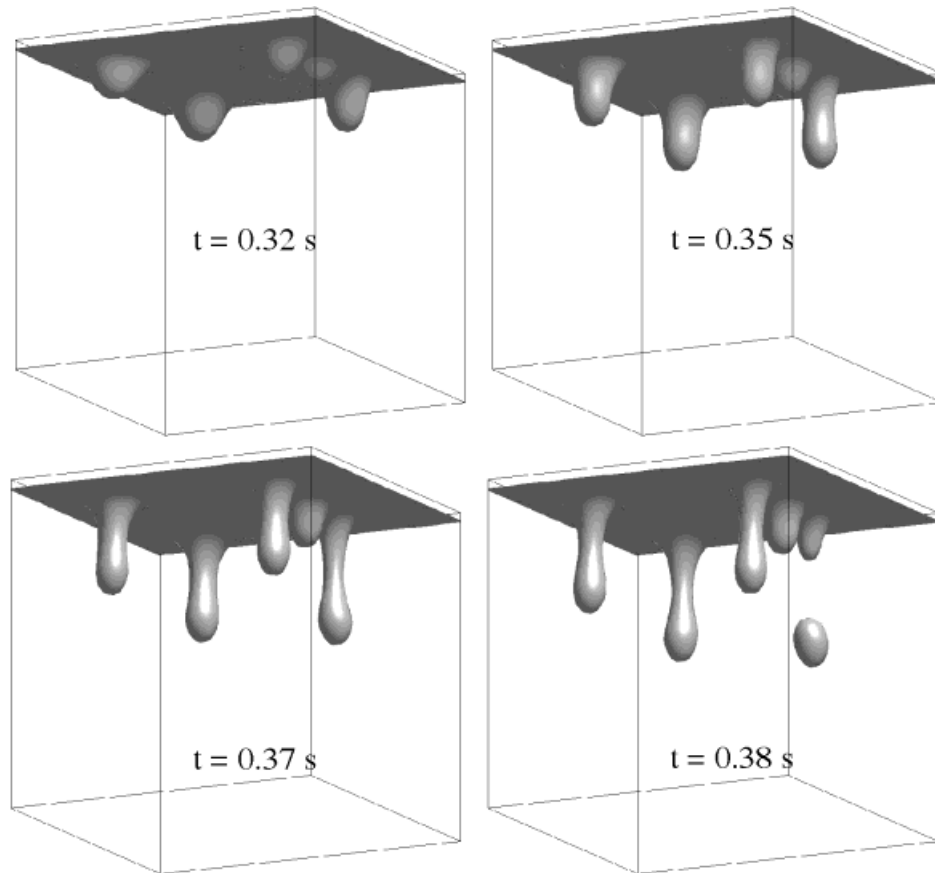


Fig. 4. Evolution of a lead film surface on a downward-facing first wall with random initial perturbation.

perturbation with maximum amplitude of 1.0 mm is applied at the beginning of the transient. These results suggest that droplet detachment occurs nearly 0.38 s after the initial perturbation is imposed. This is to be considered in relation to the time between shots of ~ 0.2 s (corresponding to a repetition rate of ~ 5 Hz) anticipated for a power plant.

Generalized nondimensional charts for the droplet detachment time as a function of the initial thickness, injection velocity, Reynolds number, and surface mass flux have been developed; a typical chart is shown in Fig. 5. The length and timescales are defined by the relations

$$l = \left(\frac{\sigma}{g(\rho_L - \rho_G)} \right)^{1/2} \quad (1)$$

and

$$t_o = \left(\frac{l}{g} \right)^{1/2}, \quad (2)$$

where

σ = surface tension of the liquid

ρ_L, ρ_G = liquid and gas densities, respectively

g = gravitational acceleration.

For reference, the corresponding values for lead at 700 K are 2.14 mm and 14.8 ms, respectively.¹¹

Charts similar to that shown in Fig. 5 for other values of the nondimensional initial film thickness and injection velocity may be found in Ref. 11. Referring to Fig. 5, for a given coolant, wall porosity, coolant delivery system design, and operating conditions (i.e., Reynolds number, injection velocity, film thickness, and evaporation/condensation rate), one can determine the minimum time required for a liquid drop to form and detach from the perturbed film surface. Since the liquid film is expected to be completely disrupted following an explosion, the subsequent explosion should be initiated during the time window between the point when film coverage is reestablished and the point when drops begin “raining” into the cavity, thereby interfering with target and/or beam

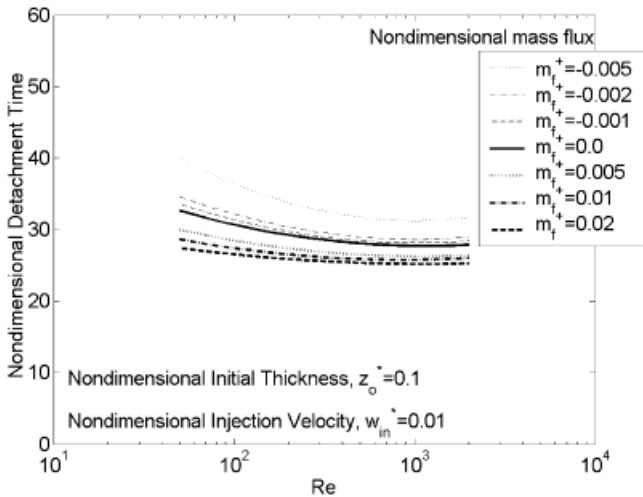


Fig. 5. Typical generalized nondimensional chart for the droplet detachment time. [The nondimensional detachment time, initial thickness z_o^* , and injection velocity w_{in}^* have been normalized to t_0 from Eq. (2), l in Eq. (1), and l/t_0 , respectively; the nondimensional mass flux m_f^+ is defined as the ratio between the evaporation/condensation mass flux at the interface and the product of the liquid density and the characteristic velocity l/t_0 . Positive values correspond to condensation, while negative values correspond to evaporation.]

propagation. Hence, these results suggest that liquid-film stability may impose a limit on the minimum repetition rate in order to avoid liquid “dripping” into the chamber between shots.

Generalized charts have also been developed for the minimum film thickness during the evolution of the free surface prior to droplet detachment and for the equivalent diameter of the detached droplets as functions of the initial film thickness, injection velocity, Reynolds number, and nondimensional mass flux at the interface (due to condensation or evaporation). These results indicate that at low injection velocities, the film thickness in the immediate vicinity of the growing liquid “spikes” (i.e., droplets) may decrease well below the nominal mean film thickness value over the entire surface. In extreme cases, the liquid film may rupture, causing dry patches to form. Therefore, these results suggest that a minimum injection velocity will be required to prevent the film thickness from decreasing below a designer-specified minimum value dictated by wall protection requirements. The generalized charts reported in the companion paper¹¹ can therefore be used to define the operational and design windows necessary for successful operation of the wetted-wall concept. A preliminary experimental investigation aimed at validating the model has been performed. The data show good agreement with model predictions.

For the forced-film-flow wall protection concept, film detachment under the influence of gravity is most likely to occur on the downward-facing surfaces in the upper part of the reactor chamber. Film detachment and uncontrolled “fall-out” would likely interfere with beam propagation and/or target injection. It would also negate the protective function of the film. Hence, an experimental study has been performed to determine the effect of various design and operational parameters on the film detachment distance downstream of the introduction point for downward-facing flat surfaces with various inclination angles. Experiments were conducted for both wetting and nonwetting surfaces with different initial film thicknesses (1.0 to 2.0 mm), initial film injection velocities (1.9 to 11.0 m/s), and inclination angles (0 to 45 deg).

Figure 6 provides typical results for the film detachment distance normalized by the initial film thickness (x_d/δ) as a function of the Froude number Fr for both wetting (glass) and nonwetting (Rain-X coated glass) horizontal downward-facing surfaces, where

$$Fr = \frac{U}{(g\delta \cos \theta)^{1/2}}, \quad (3)$$

where

U = initial film velocity

g = gravitational acceleration

θ = inclination angle.

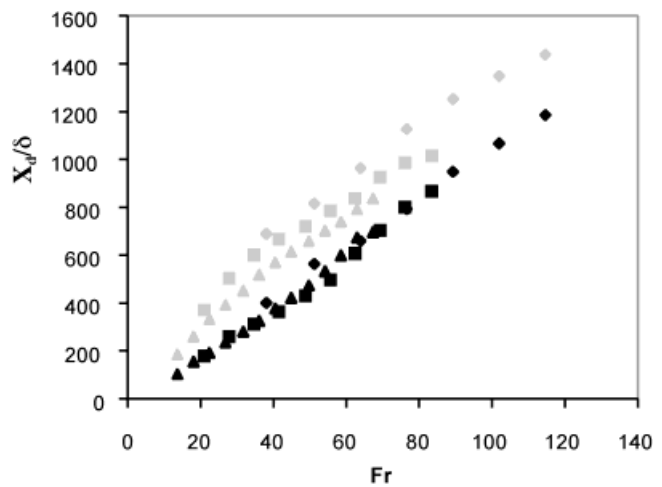


Fig. 6. Variation of the normalized film detachment distance with Froude number for horizontal downward-facing surfaces [light symbols = wetting surface; dark symbols = nonwetting surface; δ = 1.0, 1.5, and 2.0 mm (diamonds, squares, and triangles)].

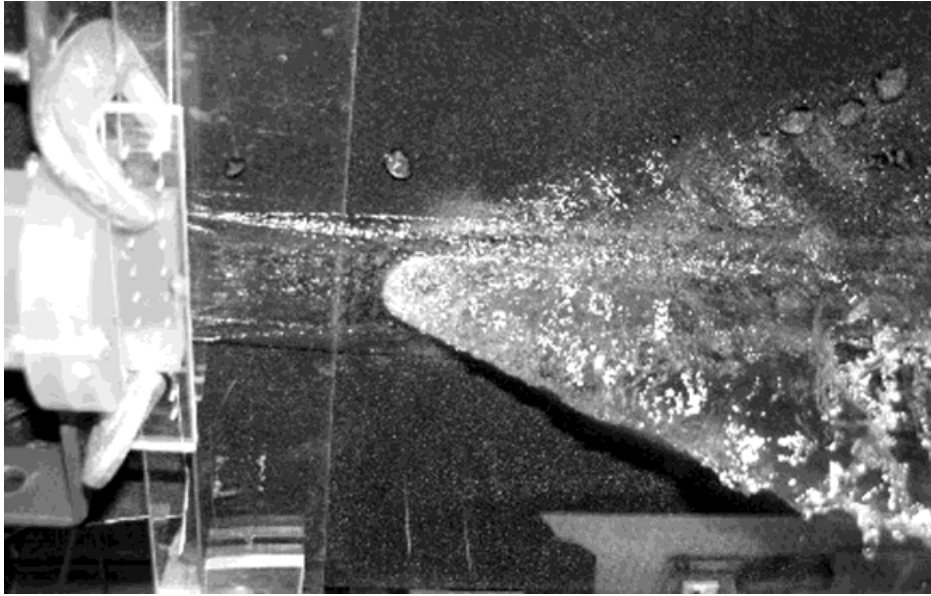


Fig. 7. Flow of a 1.5-mm-thick film with a 5.0 m/s velocity around a 25.4-mm-diam, 2.4-mm-high cylindrical “port.”

Similar data for other inclination angles may be found in Ref. 12.

The data suggest that the normalized detachment distance strongly depends on the Froude number and surface characteristics (i.e., wettability). The data shown in Fig. 6 for a nonwetting horizontal surface provide a lower bound for the detachment distance. These data allow the designers to establish the maximum allowable spacing between film injection and liquid return points along the cavity surface to avoid film detachment.

Experiments have also been performed to examine the behavior of thin liquid films flowing around cylindrical obstacles, typical of the protective dams shielding beam and target injection ports. Results for a 1.5-mm-thick film flowing past a 25.4-mm-diameter, 2.4-mm-high cylindrical obstacle with a velocity of 5.0 m/s are shown in Fig. 7. These results indicate that the presence of such obstacles will pose a significant challenge to the designers, inasmuch as the disrupted film may directly interfere with the intended function of the port (namely, beam propagation or target injection). Hence, efforts are currently under way to examine the behavior of thin films flowing past “streamlined” obstacles.

IV. CHAMBER CONDITIONS

Preshot chamber conditions must satisfy the driver propagation and focusing requirements along with the target integrity and delivery requirements. In addition to the conditions of the chamber gas/vapor governed by evaporation and film condensation, the possible presence

of aerosol must be considered. The major processes involved are those providing the source terms for aerosol formation (both from the high-power deposition at the wall and from subsequent in-flight recondensation) and the aerosol behavior between shots.

IV.A. Film Condensation

The net film condensation can be expressed by the difference between the condensation flux to the wall and the evaporation flux from the wall and can be expressed as follows¹³:

$$j_{net} = \left(\frac{M}{R2\pi} \right)^{0.5} \left[\Gamma \sigma_c \frac{P_g}{T_g^{0.5}} - \sigma_e \frac{P_f}{T_f^{0.5}} \right], \quad (4)$$

where

M = molecular weight of the gas

R = gas constant

T_g = gas temperature

P_g = gas pressure

T_f = liquid temperature

P_f = liquid pressure (corresponding to the saturation pressure at T_f)

σ_c = condensation coefficient

σ_e = evaporation coefficient

Γ = factor to account for the motion of the gas toward or away from the wall.

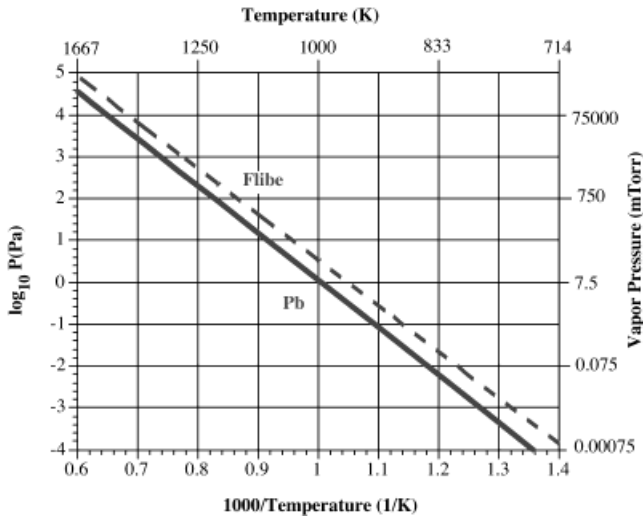


Fig. 8. Vapor pressure as a function of temperature for lead (from Ref. 2) and for flibe (based on Ref. 14).

The classical exponential vapor pressure variation with temperature is shown in Fig. 8 for lead (from Ref. 2) and for flibe (based on Ref. 14).

A characteristic condensation time based on condensation rate and corresponding vapor mass in the chamber was used to estimate the time required for film condensation to clear the chamber as a function of vapor pressure and temperature for both lead and flibe. For simplicity, the calculations do not include the effect of vapor velocity toward or away from the wall [$\Gamma = 1$ in Eq. (4)]. This effect could change the rate of condensation by as high as a factor of ~ 3.6 and as low as a factor of ~ 0.09 for sonic-speed-like velocities toward and away from the wall, respectively.¹³ Example results are shown in Fig. 9

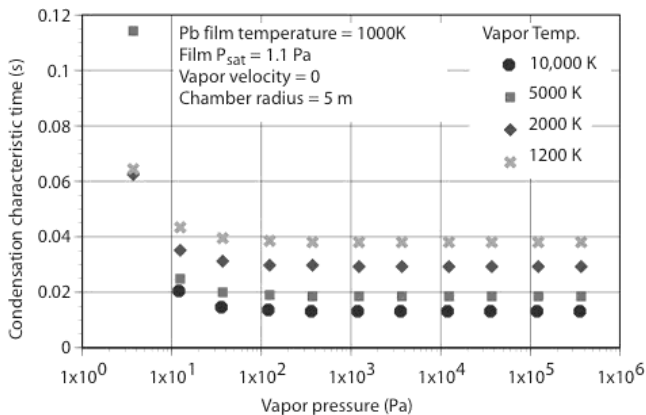


Fig. 9. Characteristic condensation time for lead vapor as a function of vapor temperature and pressure for a film temperature of 1000 K and a chamber radius of 5 m.

for a lead film temperature of 1000 K and a chamber radius of 5 m.

From Fig. 9, for a given vapor temperature, the characteristic condensation time is virtually independent of the vapor pressure until it decreases to within about one order of magnitude of the saturation pressure corresponding to the liquid-film temperature. For all lead vapor temperatures considered, this characteristic time (< 0.04 s) is considerably smaller than the time between shots (0.1 to 1 s), which shows that condensation itself is fast. The overall film condensation process in a chamber would probably be more limited by vapor transport to the wall (e.g., through convection or diffusion) and by the heat transfer effectiveness of the wetted wall to the coolant. However, the vapor pressure prior to each shot will be higher than the film saturation pressure by up to a factor of ~ 10 . Similar results were obtained for flibe (in this case P_{sat} at 800 K = 0.0063 Pa).

IV.B. Liquid-Film Ablation

For the indirect-drive-target case, a large fraction of the energy is carried by photons (see Table I) and would reach the wall in ~ 10 ns. The photon energy deposition would occur over a very short time (subnanoseconds), giving rise to very high heating rates, analogous to laser material ablation. The boiling process (surface evaporation, heterogeneous nucleation, and/or homogeneous nucleation) is dictated by the magnitude of the heating rate.¹⁵ For example, surface evaporation flux ($\text{kg/m}^2 \cdot \text{s}$) can be estimated as $-j_{net}$ from Eq. (4). The receding liquid/vapor boundary velocity under surface evaporation along coordinate r is given by

$$\frac{dr}{dt} = -\frac{j_{net}}{\rho} \quad (5)$$

The heating rate γ of the liquid-vapor interface is given by

$$\gamma = \frac{dT_f}{dt} \quad (6)$$

For constant heating rate, and substituting for j_{net} from Eq. (4) under the assumption of negligible condensation, one can rearrange Eq. (5) as follows:

$$dr = \left(\frac{M}{R2\pi} \right)^{0.5} \left[\sigma_e \frac{P_f}{T_f^{0.5}} \right] \frac{dT_f}{\gamma} \quad (7)$$

For a given expression for the fluid saturation pressure as a function of temperature, Eq. (7) can be integrated to estimate the amount of surface evaporation as a function of temperature for different heating rates. The results are illustrated in Fig. 10 in terms of the fractional evaporated fluid loss for a 0.1-mm lead film. Also shown in Fig. 10 are the typical heating rates corresponding to the photon and ion energy depositions for

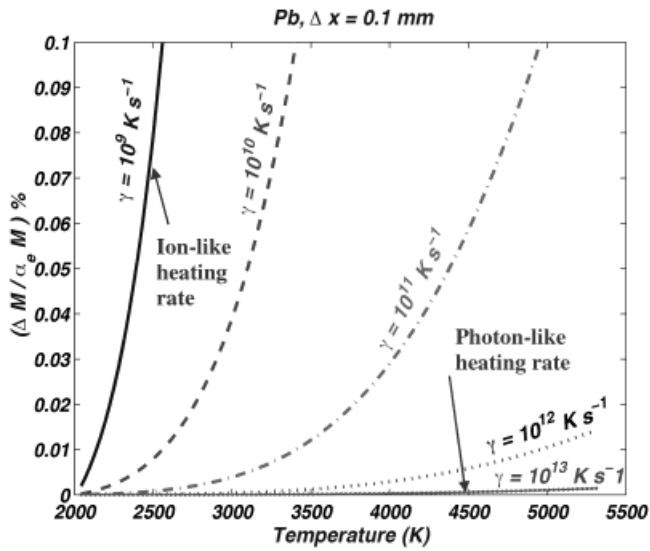


Fig. 10. Fractional surface evaporation of a 0.1-mm-thick lead film as a function of temperature for different heating rates γ .

the indirect-drive-target threat spectra. Clearly, the heating rates produced by the photons are extremely high, so that the surface evaporation process does not have sufficient time to occur; hence, it is expected to play only a minor role. However, it would play a major role for heating rates corresponding to the ion energy deposition.

Results reported in Ref. 15 for heterogeneous nucleation indicate that it would also play a minor role under extremely high (photonlike) heating rates. Instead, for such extremely high heating rates, the boiling process is dominated by homogeneous nucleation, which leads to “explosive boiling.” This involves rapid superheating to a metastable liquid state with a large excess free energy, which decomposes explosively into liquid and vapor phases. Reference 15 indicates that under these conditions, as the temperature approaches $\sim 90\%$ of the critical temperature, an avalanche-like explosive growth in the homogeneous nucleation rate (by 20 to 30 orders of magnitude) leads to this explosive boiling. A discussion of more detailed estimates of explosive boiling is given in Ref. 16. Here, for simplicity the 90% critical-temperature criterion is used to provide bounding estimates of the amount of material ablated by the photon energy deposition, as illustrated in Figs. 11 and 12 for lead and flibe, respectively, for a chamber radius of 6.5 m.

Figure 11 shows the spatial profile of the photon energy deposition within a lead film. Normally, this would cause part of the liquid film to be vaporized (where the energy deposited exceeds the sensible heat plus the latent heat of vaporization). It would also result in a two-phase region (where the energy deposited is lower than the above case but still exceeds the sensible heat). It is not

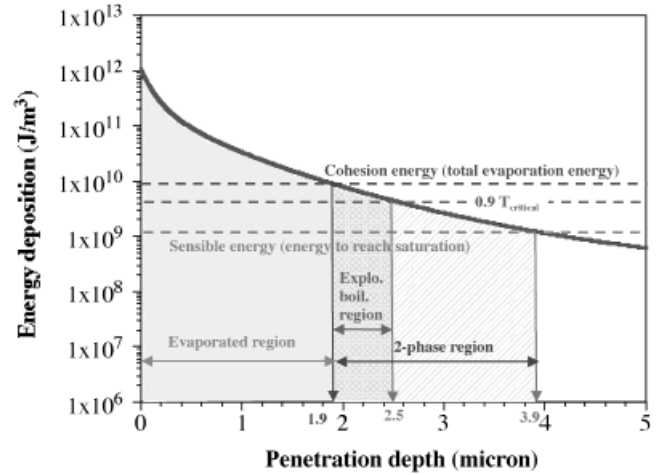


Fig. 11. Volumetric heat deposition in a lead film in a chamber of radius 6.5 m from 458-MJ indirect-drive photon spectra illustrating two-phase region and regions where explosive boiling is likely to occur, assuming that the pressure of the ablated lead at the interface is 1000 torr.

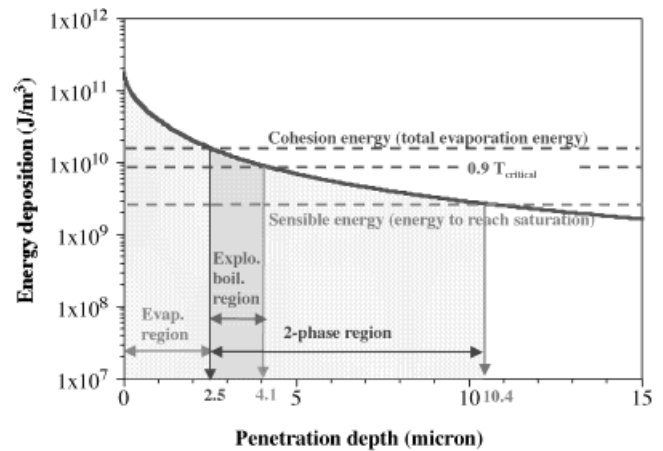


Fig. 12. Volumetric heat deposition in a flibe film in a chamber of radius 6.5 m from 458-MJ indirect-drive photon spectra illustrating two-phase region, assuming that the pressure of the ablated flibe at the interface is 1000 torr.

clear to what extent this two-phase region will ablate or remain on the surface. Superimposing a line corresponding to 90% of the critical temperature (as suggested by Ref. 15) shows the explosive boiling region that will be ablated. Two bounding estimates of ablated material can then be inferred as a source term for aerosol calculations: an upper bound assuming all material in the two-phase region to be ablated and a lower-bound case assuming all material undergoing explosive boiling to be ablated. Similar results for a flibe film are shown in Fig. 12. The size

of the chamber is an important parameter as it determines the wall surface area seen by the photons. For example, reducing the chamber radius from 6.5 to 3.5 m results in an increase in the explosive boiling region thickness from 2.5 to 3.8 μm for lead and from 4.1 to 10.9 μm for flibe.

The film ablation due to explosive boiling would generate an impulse, which would create a shock wave in the film that depending on the liquid and reflecting wall acoustic impedances could be followed by a rarefaction wave. If the net tensile stress in the liquid due to this rarefaction wave is higher than the spall strength of the liquid, spalling would occur that would provide an additional source of ablated material for aerosol formation on the chamber. A more detailed discussion of this potential ablation mechanism is given in Ref. 16. An estimate for a flibe film on a ferritic steel wall in a chamber with a radius of 6.5 m indicates an additional ablation due to spallation of $\sim 3.1 \mu\text{m}$ (compared to 4.1 μm from explosive boiling).¹⁶ Such a spallation analysis depends on a number of parameters such as the liquid and structure materials, the shock-wave magnitude and profile, and the local spalling strength characteristics of the liquid. Further study is needed to better understand this phenomenon for IFE materials (such as flibe) under relevant shock conditions as it could provide an additional source term for aerosol formation.

X-ray energy deposition and wall evaporation analysis were also carried out with BUCKY, a one-dimensional Lagrangian radiative hydrodynamic simulation code.¹⁷ For these calculations, radiative transfer was approximated using multigroup flux-limited diffusion with opacity information generated with a collisional-radiative rate equation solver in the average atom approximation. For the heavy-ion-beam-driven target, the bulk of the threat is from the large flux of soft X rays (less than $\sim 1 \text{ keV}$). The dense ionized vapor formed by the interaction of the early part of the X-ray pulse shields the surface from later X rays and ions, reradiating the absorbed energy in timescales long compared to the pulse from the target. The BUCKY simulations were run out to 1 μs , and the resulting chamber conditions were used to generate input for further aerosol analysis.

To contrast the source terms of aerosol formation for the two types of target considered, BUCKY simulations were performed for a chamber of radius 4.5 m, initially filled with lead vapor of density corresponding to a pressure of 1 mtorr at standard room temperature and protected by a 1-mm lead film for the 154-MJ laser-driven direct-drive target and the 458-MJ heavy-ion-beam-driven indirect-drive target. The absorption opacity of the tenuous lead vapor and of the lead liquid as well as the emission opacity of the resultant high-density, low-temperature lead plasma were calculated using IONMIX, which approximates the atomic physics by a screened hydrogenic approximation and solves the collisional radiative equations to determine the nonlocal thermodynamic equilibrium level populations and ion-

ization stages. The insult posed by the heavy-ion-beam indirectly driven target, dominated by soft X rays, caused 21.4 kg of lead to vaporize ($\sim 7.4 \mu\text{m}$) and a maximum overpressure of $1.5 \times 10^4 \text{ J/cm}^3$ to the wall in reaction to the rapid evaporation of the lead. Of the 22 MJ of energy in target ions, only 5.3 MJ are deposited in the liquid as opposed to the vapor, with none penetrating further than $\sim 0.65 \mu\text{m}$ into the liquid. In contrast, the insult posed by the laser directly driven target dominated by target ion debris and burn products caused 9.2 kg of lead to vaporize ($\sim 3.2 \mu\text{m}$) and a maximum overpressure of $1.8 \times 10^3 \text{ J/cm}^3$ to the wall in reaction to the slower evaporation of the lead. These numbers form a lower bound on the amount of wall material ablated in the chamber as BUCKY does not simulate splashing or liquid carried into the chamber by the force of explosive boiling.

BUCKY is a one-dimensional radiative hydrodynamic simulation code. In these simulations, the chamber is assumed to be a perfect sphere. The relevance of a one-dimensional simulation of chamber response past the time when the vapor ejected from the wall meets the shock of the lead chamber vapor pushed outward from the target chamber center is questionable. Rather than continuing the simulations past this point, the chamber conditions at the time (internal energy, vapor density) were homogenized, and the resulting chamber was allowed to relax, with the vapor recondensing on the wall. In BUCKY, the vaporization and condensation rates are calculated using the kinetic theory model described by Labuntsov and Kryukov.¹⁸ The combination of these simulations leads to an optimistic chamber response, with no aerosolization and no liquid injected into the chamber due to drops or explosive boiling. In the case of the indirectly driven heavy-ion-beam target, the results indicate that the initial lead density assumed in the chamber (1 mtorr at room temperature) is restored within 0.15 s following chamber homogenization. Thus, for this optimistic simulation, reestablishment of the 1 mtorr (at room temperature) lead chamber conditions before the next shot is achieved for a 5-Hz repetition rate.

IV.C Aerosol Formation and Behavior

The initial state and source term parameters obtained from the analysis described in Sec. IV.B are supplied to a model¹⁹ that calculates aerosol formation rates and transport behavior. Evolution of an aerosol population is influenced by several mechanisms, such as homogenous nucleation, heterogeneous nucleation, coagulation, convection, and deposition. The aerosol dynamic equation balances the contribution from each mechanism:

$$\frac{\partial n}{\partial t} + \nabla \cdot (n\vec{v}) = \nabla \cdot (D\nabla n) + \left[\frac{\partial n}{\partial t} \right]_{\text{growth, homo}} + \left[\frac{\partial n}{\partial t} \right]_{\text{growth, hetero}} + \left[\frac{\partial n}{\partial t} \right]_{\text{coag}} - \nabla \cdot \vec{c}n, \quad (8)$$

where

n = particle density distribution function with units of number of particles per volume of particle per volume of gas ($\#/m^3/m^3$)

\vec{v} = velocity of the fluid within which the aerosol is dispersed

D = diffusion coefficient from Brownian motion of the aerosol particles.

The bracketed terms represent the rate of change in the aerosol size distribution due to particulate growth (homogeneous and heterogeneous) and particulate coagulation. The final term on the right side represents the rate at which aerosol particles are removed from the system because of external forces. If the external forces and the resulting drag force are in equilibrium, then \bar{c} is the terminal velocity of the particles. For the study presented here, diffusion and deposition are not considered since they generally impact an aerosol population on time-scales larger than the typical IFE intershot frequency.

At locations with sufficient supersaturation, aerosol particles may condense by homogeneous nucleation. The rate that particles nucleate per unit volume is determined from classical nucleation theory¹⁹:

$$\left[\frac{\partial n}{\partial t} \right]_{\text{growth, homo}} = \left(\frac{P_{\text{sat}}}{kT} \right)^2 \left(\frac{2\sigma m}{\pi} \right)^{1/2} \frac{S^2}{\rho_l} \times \exp \left[-\frac{\pi\sigma d_{\text{crit}}^2}{3kT} \right] \delta(V_{\text{crit}}) \quad (9)$$

with

$$d_{\text{crit}} = \frac{4\sigma m}{\rho_l kT \ln S}$$

and

$$V_{\text{crit}} = \frac{\pi}{6} d_{\text{crit}}^3,$$

where

P_{sat} = vapor saturation pressure over a flat surface infinite in extent (J/m^3)

k = Boltzmann constant

T = local vapor temperature (K)

σ = surface tension of a condensed droplet of the material (J/m^2)

m = mass of a vapor atom (kg)

ρ_l = liquid phase density of the material (kg/m^3)

and S is called the saturation ratio and is defined as $S = P/P_{\text{sat}}$ with P representing the local vapor pressure. The delta function is necessary to place the nucleated aerosol

at the correct position in particulate volume space when describing the rate of change of the particulate distribution function n . The two remaining parameters, d_{crit} and V_{crit} , are the critical size and volume at which the condensation and evaporation rates of the cluster are equal.

Once formed, the particles grow by heterogeneous nucleation (or vapor deposition) and agglomeration, and they experience convection due to the velocity of the remaining vapor in the chamber. Heterogeneous nucleation depends on state properties of the condensing vapor, and the growth rate is given by¹⁹

$$\left[\frac{\partial n}{\partial t} \right]_{\text{growth, hetero}} = -\frac{\partial}{\partial(V)} \left(n 2\pi \left(\frac{\pi}{6} \right)^{1/3} \frac{(S-K)P_{\text{sat}} D d_p}{kT} V_{\text{mol}} F \right), \quad (10)$$

where

K = correction factor for the curvature of a particle with diameter d_p

V_{mol} = volume of a single molecule of the condensing species

F = correction factor allowing interpolation between free-molecular and continuum flow regimes.

Coagulation describes the process of two particles (or droplets) colliding to become one particle with a volume equal to the sum of the volumes of the initial particles. The rate of growth of the aerosol population by coagulation is given as¹⁹

$$\left[\frac{\partial n}{\partial t} \right]_{\text{coag}} = \frac{1}{2} \int_0^V \beta(V^*, V - V^*) n(V^*) n(V - V^*) dV^* - \int_0^\infty \beta(V, V^*) n(V) n(V^*) dV^*, \quad (11)$$

where $\beta(V, V^*)$ is called the coagulation kernel and depends on colliding particle sizes and system thermodynamic properties.¹⁹

The model used to calculate properties of the aerosol population in IFE postshot chamber conditions solves the aerosol dynamic equation with the rates given above. Other mechanisms, such as ion-induced nucleation, are likely important in the chamber environment and will be included in future work. Solution to the aerosol dynamic equation is coupled with a gas-dynamics model that calculates the state variables.¹⁹ The models are constructed to ensure conservation of energy and mass; i.e., mass and energy are exchanged between vapor and aerosol as particles condense or evaporate. Once formed, the particles grow by vapor deposition and agglomeration, and they experience convection due to the velocity of the remaining vapor in the chamber. The model also calculates vapor mass lost to recondensation onto the wall.

When an aerosol particle (or droplet) strikes the chamber wall, it can be either reflected or absorbed to some extent by the wall depending on its size, velocity, and incident angle and on the wall conditions. For example, a droplet hitting a liquid surface would result in liquid expulsion from the wall, the mass of which in relation to the mass of the impacting droplet would define the net mass reflection and absorption (coagulation) by the wall. Detailed information is not available on the behavior of flibe or lead droplets hitting a liquid wall under IFE-like conditions. However, it is possible to make some bounding estimates. For example, the assumption of a fully reflective wall would provide a conservative illustration of the total amount of aerosol formed in the absence of coagulation with the liquid wall and would show how the aerosol size and number density evolve during the chamber relaxation period. The wetted-wall chamber behavior following ablation from the IFE photon energy deposition was analyzed under this assumption. Future work should include experimental and modeling studies of the effect of liquid droplets impacting a liquid wall for candidate IFE materials (such as flibe and lead) to help in better characterizing and understanding the aerosol behavior.

Results of the aerosol calculations at the center region of a chamber with a flibe wetted wall are summarized in Figs. 13 and 14 for chamber radii of 6.5 and 3 m under the simplifying assumption of single-component aerosol and condensation behavior for flibe. The initial ablation source terms assumed for the calculations (5.5 and 11.5 μm) are similar to the lower-bound explosive boiling source term described in Sec. IV.B. Heating from ions that arrive later in time were not considered for this estimation. The aerosol mass for the 6.5-m-chamber-

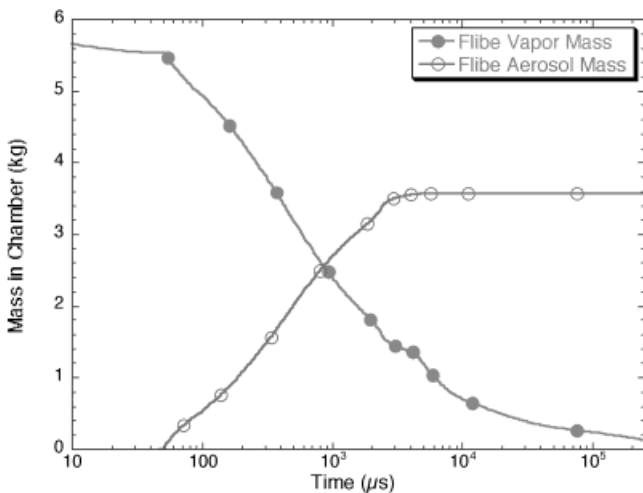


Fig. 13. Flibe aerosol and vapor mass history in 6.5-m-radius chamber following a shot (assuming an ablated thickness of 5.5 μm).

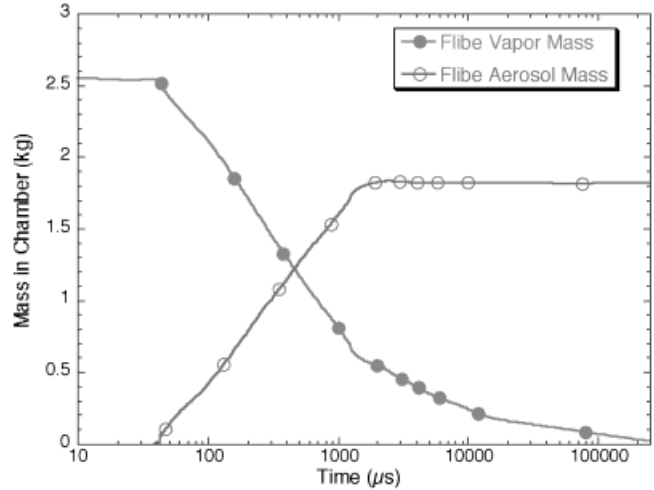


Fig. 14. Flibe aerosol and vapor mass history in 3-m-radius chamber following a shot (assuming an ablated thickness of 11.5 μm).

radius case increases to ~ 3.5 kg within a few milliseconds and stays roughly constant thereafter as no wall coagulation (possible sink term) is assumed. The vapor pressure decreases continuously because of condensation on the wall. A similar trend is observed for the 3-m-chamber-radius case with the aerosol mass increasing to ~ 1.8 kg within a few milliseconds.

Figure 15 shows the aerosol particle size distribution in the inner chamber region at various times for a chamber radius of 3 m. Figure 15 illustrates the growth of particles with time due to condensation and particle

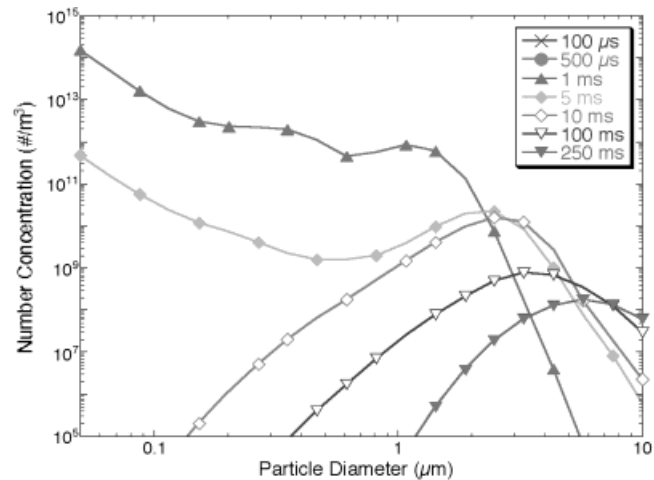


Fig. 15. Example of time evolution of flibe aerosol characteristics in the center of the chamber following a shot for a chamber radius of 3 m.

coagulation and the corresponding decrease in particle density. From these results after ~ 0.25 s (about the time between each IFE shot), there are still $\sim 10^9$ to 10^{10} aerosol droplets/m³ dispersed throughout the chamber volume with sizes of ~ 1 to $10 \mu\text{m}$. Similar results were obtained for the 6.5-m-chamber-radius case except that the particles after 0.25 s tended to be smaller, ~ 0.5 to $5 \mu\text{m}$. These results are illustrative and do not include processes enhancing chamber clearing, such as aerosol coagulation with the liquid wall, but clearly illustrate the potential for aerosol formation and growth. Aerosol remnants prior to the next shot in combination with the chamber vapor pressure could affect the driver firing and/or target injection, as is discussed in more detail in Ref. 3. This is an area where there are still many uncertain parameters, such as the coagulation and reflection behavior of droplets of different sizes and velocities impacting a liquid wall, and that needs to be addressed through future experimental and modeling effort.

V. CONCLUSIONS

A thin-liquid-film-wall configuration for IFE provides the possibility of high efficiency and renewable armor. Key issues include film reestablishment and coverage, and aerosol formation and behavior relative to the preshot chamber conditions dictated by target and driver requirements. These issues have been investigated, and key results are reported in this paper.

Analysis of wetted-wall reestablishment and coverage indicates that (a) liquid-film stability may impose a limit on the minimum repetition rate in order to avoid liquid "dripping" into the chamber between shots and (b) a minimum injection velocity will be required to prevent the film thickness from decreasing below a minimum value dictated by wall protection requirements. Analysis of thin-liquid-film forced flow indicates that the normalized detachment distance strongly depends on the Froude number and surface characteristics (i.e., wettability). Efforts in the film dynamics area include generation of generalized charts to help system designers establish parametric design windows.

Liquid-wall ablation is important for an indirect-drive-target case because of the large amount of photon energy that is deposited over a short time (approximately nanoseconds). The heating rates are comparable to laser material ablation cases from whose studies and experiments IFE ablation processes can be inferred. Under such high heating rates, surface evaporation and heterogeneous nucleation play a minor role in the boiling process. Instead, homogeneous nucleation is the dominant process. The liquid is rapidly superheated to a metastable liquid state with an excess free energy. At temperatures approaching $\sim 90\%$ of the critical temperature, avalanche-like explosive growth in the homogeneous nucleation

rate (by 20 to 30 orders of magnitude) occurs, which leads to the explosive decomposition of the superheated liquid into liquid and vapor phases (also referred to as spinoidal decomposition). This is an area where much remains to be learned. For instance, it is not clear what the form of the ejecta is (vapor, liquid droplet size, and distribution). Future studies of IFE candidate liquid-wall materials (such as flibe and lead) under such conditions are needed. For example, simulation of the photon energy deposition in X-ray and/or laser facilities under IFE-like heating rates and deposition profiles and with the right diagnostics capabilities would greatly help in further understanding this process.

An additional ablation term could result from the shock wave imparted on the liquid film by the explosive boiling ejecta. Depending on the liquid and reflecting wall acoustic impedances, this shock wave could be followed by a rarefaction wave, resulting in spalling if the net tensile stress in the liquid is higher than its spall strength. This is another area requiring future experimental and modeling effort to help in better understanding the behavior of IFE materials under such conditions.

Bounding estimates of liquid-wall ablation based on explosive boiling were made for use as source terms in subsequent aerosol analysis. Such analysis of aerosol behavior indicates that a significant amount of aerosol would be formed and, depending on the wall boundary conditions, could be present prior to each shot. The combination of aerosol and vapor in the chamber at that time must be compatible with driver firing and target injection requirements, as discussed in Ref. 3. The aerosol modeling performed for this study relies on simplifying assumptions, such as the assumption of a fully reflective liquid-wall surface and the absence of particle slips. Further modeling and experimental efforts are needed to better understand and assess aerosol formation and behavior for candidate wetted-wall materials under IFE conditions.

ACKNOWLEDGMENT

This work was supported by the U.S. Department of Energy under contract DE-FC03-95ER54299.

REFERENCES

1. M. J. MONSLER et al., "An Overview of Inertial Fusion Reactor Design," *Nucl. Technol. Fusion*, **1**, 302 (1981).
2. L. M. WAGANER et al., "Inertial Fusion Energy Reactor Design Studies, PROMETHEUS-L, PROMETHEUS-H," DOE/ER-54101, MDC 92E0008, McDonnell Douglas Aerospace (Mar. 1992).
3. F. NAJMABADI, A. R. RAFFRAY, and ARIES TEAM, "Operational Windows for Dry-Wall and Wetted-Wall IFE Chambers," *Fusion Sci. Technol.*, **46**, 401 (2004).

4. R. MOIR et al., "HYLIFE-II: A Molten-Salt Inertial Fusion Energy Power Plant Design—Final Report," *Fusion Technol.*, **25**, 5 (1994).
5. D. T. GOODIN, N. B. ALEXANDER, C. R. GIBSON, A. NOBILE, R. W. PETZOLDT, N. P. SIEGEL, and L. THOMSON, "Developing Target Injection and Tracking for Inertial Fusion Energy Power Plants," *Nucl. Fusion*, **41**, 527 (2001).
6. S. E. BODNER, D. G. COLOMBANT, A. J. SCHMITT, and M. KLAPISCH, "High-Gain Direct-Drive Target Design for Laser Fusion," *Phys. Plasmas*, **7**, 6, 2298 (2000).
7. "ARIES-IFE Reference Target Spectra," available on the Internet at <http://aries.ucsd.edu/ARIES/WDOCS/ARIES-IFE/SPECTRA/>.
8. D. A. CALLAHAN-MILLER and M. TABAK, "Increasing the Coupling Efficiency in a Heavy Ion, Inertial Confinement Fusion Target," *Nucl. Fusion*, **39**, 7, 883 (July 1999).
9. M. S. EL-GENK and H. H. SABER, "Minimum Thickness of a Flowing Down Liquid Film on a Vertical Surface," *Int. J. Heat Mass Transfer*, **44**, 2809 (2001).
10. S. I. ABDEL-KHALIK and M. YODA, "Design Considerations for Thin Liquid Film Wall Protection Systems," presented at ARIES Project E Meeting, October 17–24, 2001, available on the Internet at <http://aries.ucsd.edu/ARIES/MEETINGS/0110/>.
11. S. SHIN, S. I. ABDEL-KHALIK, D. JURIC, M. YODA, and ARIES TEAM, "Effects of Surface Evaporation and Condensation on the Dynamics of Thin Liquid Films for the Porous Wetted Wall Protection Scheme in IFE Reactors," *Fusion Sci. Technol.*, **44**, 117 (2003).
12. J. K. ANDERSON, S. G. DURBIN II, D. L. SADOWSKI, M. YODA, S. I. ABDEL-KHALIK, and ARIES TEAM, "Experimental Studies on High-Speed Liquid Films over Downward-Facing Surfaces for Inertial Fusion Energy Wet Wall Concepts," *Fusion Sci. Technol.*, **43**, 401 (2003).
13. J. G. COLLIER, *Convective Boiling and Condensation*, 2nd ed., McGraw-Hill, New York (1981).
14. M. R. ZAGHLOUL, D. K. SZE, and A. R. RAFFRAY, "Thermophysical Properties and Equilibrium Vapor Composition of Lithium-Fluoride Beryllium-Fluoride (LiF/BeF₂) Molten Salt," *Fusion Sci. Technol.*, **44**, 344 (2003).
15. W. FUCKE and U. SEYDEL, "Improved Experimental Determination of Critical-Point Data for Tungsten," *High Temp.-High Pres.*, **12**, 419 (1980).
16. M. ZAGHLOUL and A. R. RAFFRAY, "IFE Liquid Wall Response to the Prompt X-Ray Energy Deposition: Investigation of Physical Processes and Assessment of Ablated Material," *Fusion Sci. Technol.* (accepted for publication).
17. R. R. PETERSON et al., "The BUCKY and ZEUS-2D Computer Codes for Simulating High Energy Density ICF Plasmas," *Fusion Technol.*, **30**, 783 (1996).
18. D. A. LABUNTSOV and A. P. KRYUKOV, "Analysis of Intensive Evaporation and Condensation," *Int. J. Heat Mass Transfer*, **22**, 989 (1979).
19. J. P. SHARPE, B. D. MERRILL, and D. A. PETTI, "Modeling of Particulate Production in the SIRENS Plasma Disruption Simulator," *J. Nucl. Mater.*, **290–293**, 1128 (2001).